Title   Broadband Fluorographene Photodetector

Sichao Du, Wei Lu, Ayaz Ali Hakro, Pei Zhao, Khurram Shehzad, Hongwei Guo, Lingling Ma, Xuemei Liu, Xiaodong Pi, Peng Wang, Hehai Fang, Zhen Xu, Chao Gao, Yaping Dan, Pingheng Tan, Hongtao Wang, Cheng-Te Lin, Jianyi Yang, Shurong Dong, Zhiyuan Cheng, Erping Li, Wenyan Yin, Jikui Luo, Bin Yu, Tawfique Hasan, Yang Xu,* Weida Hu,* Xiangfeng Duan

Dr. S. Du, W. Lu, A. A. Hakro, Dr. K. Shehzad, H. Guo, L. Ma, X. Liu, Prof. J. Yang, Prof. S. Dong, Prof. Z. Cheng, Prof. E. Li, Prof. W. Yin, Prof. J. Luo, Prof. Y.Xu

The Key Laboratory of Micro-Nano Electronics and Smart System of Zhejiang Province College of Information Science and Electronic Engineering

Zhejiang University

Hangzhou, Zhejiang 310027, China

E-mail: yangxu-isee@zju.edu.cn

Prof. P. Zhao, Prof. H. Wang

Institute of Applied Mechanics

Zhejiang University

Hangzhou, Zhejiang 310027, China

Prof. X. Pi

State Key Laboratory of Silicon Materials

College of Material Science

Zhejiang University

Hangzhou, Zhejiang 310027, China

P. Wang, H. Fang, Prof. W. Hu

National Laboratory for Infrared Physics

Shanghai Institute of Technical Physics

Chinese Academy of Sciences

Shanghai 200083, China

E-mail: wdhu@mail.sitp.ac.cn

Dr. Z. Xu, Prof. C. Gao

MOE Key Laboratory of Macromolecular Synthesis and Functionalization

Zhejiang University

Hangzhou, Zhejiang 310027, China

Prof. Y. Dan

Joint Institute of University of Michigan and Shanghai Jiaotong University,

Shanghai 200240, China

Prof. H. Tan

State Key Laboratory of Superlattices and Microstructures

Institute of Semiconductors

Chinese Academy of Sciences

Beijing 100083, China

Prof. C.-T. Lin

Key Laboratory of Marine Materials and Related Technologies

Zhejiang Key Laboratory of Marine Materials and Protective Technologies

Ningbo Institute of Materials Technology and Engineering

Chinese Academy of Sciences,

Ningbo, Zhejiang 315201, China

Prof. B. Yu

College of Nanoscale Science and Engineering

State University of New York

New York 12203, United States

Dr. T. Hasan

Department of Engineering

University of Cambridge

Cambridge CB3 0FA, United Kingdom

Prof. X. Duan

3

Department of Chemistry and Biochemistry

University of California

Los Angeles, California 90095, United States

High-performance photodetectors operating over a broad wavelength range from ultraviolet, visible to infrared are of scientific and technological importance for a wide range of applications. In this work, a photodetector based on van der Waals heterostructures of graphene and its fluorine-functionalized derivative is presented. It consistently shows broadband photo-response from ultraviolet (255nm) to mid-infrared (4.3 μm) wavelengths, with three orders of magnitude enhanced responsivity compared to pristine graphene photodetectors. The broadband photodetection is attributed to the synergistic effects of the spatial non-uniform collective quantum confinement of sp^2 domains, and the trapping of photo-excited charge carriers in the localized states in sp^3 domains. Tunable photo-response has been achieved by controlling the nature of sp^3 sites, the size and fraction of sp^3/sp^2 domains. In addition, the photo-response due to the different photo-excited charge carriers trapping time in sp^2 and sp^3 nano-domains has been distinguished. The proposed scheme paves the way toward implementing high-performance broadband graphene-based photodetectors.

4

Author Manuscript

Photodetectors as a class of optoelectronics device have been widely employed in diverse fields, including spectroscopy,[1] telecommunication,[2] astronomy,[3] agriculture,[4] pharmaceuticals[5] and environmental monitoring.[6] In contrast to the photodetectors operating at a specific wavelength range, broadband photodetectors with photo-response to a much wider spectrum and spectrally distinctive are highly desirable, owing to its importance to a variety of applications.[7, 8] The wealth of sufficient information held in the broad spectral domain offers significant advantages over traditional

panchromatic and multispectral imagery. [9] Hence, the hyperspectral imaging has been used as a powerful technique for global climate research, wetlands mapping, mineral identification, crop analysis, and bathymetry, *etc.*.[10] In addition, two-color intelligent detection and recognition has also been under extensive investigations. For instance, ultraviolet (UV)-visible (VIS) photodetectors can meet the demands on astronomical detection,[11] wide spectral switches[12] or memory storage [13]; VIS and near-infrared (IR) photodetectors are widely used in consumer electronics,[14] video recording,[15] and remote sensing[16]; multi-band mid-IR photodetectors have attracted interests due to their numerous exciting applications, such as surveillance,[17] medical diagnostics,[18] bio-imaging,[4] and navigational aids[19].

However, studies on photodetectors mainly focused on their performance under specific wavelength range (UV, VIS, or IR). Broadband photodetectors generally have a complicated system configuration with high cost, consisting of trichroic prisms, optical filters, and charge coupled devices, *etc.*.[20] Graphene has been considered as a promising material for ultra-broadband photodetectors since its absorption spectrum covers the entire UV to terahertz wavelength.[21] However, the photo-responsivity of pristine graphene photodetectors is insufficient due to the low absorption efficiency of incident photons and the short lifetime of photo-generated carriers.[22] Furthermore, its semi-metal behavior results in substantial dark currents on account of the absence of an intrinsic gap, which is not suitable for highly-responsive photodetectors.[23] Hence, efforts have been made to fabricate graphene with plasmonic nanostructures,[24] micro-cavities,[25] silicon waveguide,[26] transition-metal dichalcogenide stacks,[27] hybridized quantum-dots[28]. Despite the excellent improved photo-responsivity, light absorption either relies on the materials, the structures or the resonant frequencies, thus still restricting the broadband spectral photodetection. Therefore, the challenge to enhance the photo-response without sacrificing the broadband characteristics still remains.

In this work, we present an ultra-broadband photodetector composed of graphene and its fluorine-functionalized derivative. In contrast to other graphene-based photodetectors, the van der Waals heterostructure efficiently improves the device performance while keeping the broadband photo-response of graphene. The re-hybridization of carbon with fluorine results in a mixture of sp^2 and sp^3 nano-domain, inducing a series of discrete quantum-confined states and a number of structural localized states for trapping photo-excited charge carriers. Tunable photo-response has been achieved by modulating the dihedral angles of sp^3 sites, the size/shape and fraction of sp^3/sp^2 domains. The photocurrent due to the different photo-excited charge carriers trapping time in sp^2 and sp^3 nano-domains has been distinguished. We demonstrated a prototype device yielding exceptional photo-responsivities over an ultra-broad spectral range.

Fluorine has been demonstrated to alter the pristine graphene from conductive semi-metal to insulator (bandgap from 0 to 4.1eV).[29] Since sp^2 hybridized carbon atom in graphene has a p_z orbital in the direction perpendicular to the basal plane forming a π and conjugated π* bond, when fluorine adatoms are adsorbed on the surface, they form covalent bonds with the carbon atoms which are re-hybridized from trigonal sp^2 to tetragonal sp^3 bonds.[30] Such transformation results in an opening of a bandgap through the removal of bands near the Fermi level of pristine graphene. Depending on the degree of fluorination, there is certain fraction of carbon is re-hybridized to sp^3 and bonded with fluorine. The remaining carbon is still sp^2 bonded with neighboring carbon atoms. This atomic and electronic feature of fluorographene with variable sp^3/sp^2 fractions offers novel functionalities for photodetectors. Therefore, we fabricated a fluorographene/graphene (FG/Gr) photodetector with a FG layer on the top of a graphene layer contacting with electrodes as shown in **Figure 1** a.

To explore the functionalities brought from the FG, photoluminescence (PL) measurements were carried out at different laser excitation wavelengths. As exhibited in Figure 1 d, it can be observed that

under 300 and 350 nm laser excitations, the PL peaks are at 518 nm. The intensity of the PL under 350 nm excitation is higher than that under 300 nm excitation. The PL peak shifts to longer wavelength as the excitation wavelength increases from 350 to 450 nm. Since there is a non-uniform coverage of fluorine, the FG can be described as a two-dimensional network of sp^2 C-C domains isolated within the sp^3 C-F_x matrix (x represents the atomic ratio between C and F indicating the coverage of fluorine), or vice versa as shown in Figure 1 b. From the Raman results (Figure S1), the average size of the sp^3 domains can be estimated from 5.34 to 13.73 nm by[31]

$$L_a(nm) = (2.4 \times 10^{-10})\lambda(nm)^4 (\frac{I_D}{I_G})^{-1} \qquad (1)$$

The optoelectronic properties are thus mainly determined by the π and π^* states of sp^2 domains, which lie within the σ–σ^* states of sp^3 domains.[32] The energy gap between π and π^* states generally depends on the size of sp^2 domain and the conjugation length. A number of sp^3 re-hybridized induced localized states n, which is related to the dihedral angle of the σ bonds, exist in the band tail of π and π^* states or lie deeper within the π - π^* gap.[33] Therefore, the PL peak at 518 nm is ascribed to an overall π and π^* transition (2.39 eV) from the sp^2 domains with a Stokes shift of 168 nm (1.15 eV). As the excitation wavelength increases, the PL spectrum gets broader and shifts to the longer wavelength due to $n\square$-$\square\pi$ transitions from sp^3 domains as depicted in Figure 1 c. The former emission bears the discrete feature due to quantum confinement of electrons inside the sp^2 domains.[34] The latter emission possesses broad absorption and emission states-band within the π - π^* gap.

The photocurrent measurements of a reference Gr/Gr device and the FG/Gr device were then conducted and compared at different laser wavelengths with a fixed irradiance (**Figure 2** a, b and Figure S2 a, b). The photocurrent ΔI of FG/Gr increases from nA to μA, with over one thousand times increase compared to Gr/Gr. Figure 2 c, d show the responsivity of these two photodetectors as a

function of incident laser irradiance at different laser wavelengths. The responsivity of FG/Gr decreases with respect to the increase of laser irradiance. It is worth mentioning that we have tested a number of FG/Gr devices and the statistical responsivities at different laser wavelengths are exhibited in **Figure 3** a-i. The observed photo-response can be explained by the operating principle and energy band structure. When the FG/Gr heterostructure is illuminated by light, the electrons in the π state could be excited forming electron−hole pairs. The presence of quantum confinement and localized states in the π-π^* gap leads to the trapping of these electrons, while the holes flow into the graphene channel *via* the built-in potential at the FG/Gr heterostructure junction, resulting in the photo-induced current.

The measured photo-response characteristics manifest a broadband detection, where the FG/Gr devices show strong photo-response in the whole tested wavelength range from 255 nm to 4.3 μm. The responsivity of FG/Gr photodetector is more than three orders of magnitude higher than that of Gr/Gr photodetector. Since various size/shape of the sp^2 domains induce spatial non-uniform quantum confinements, a series of discrete quantum-confined states from the sp^2 domains contribute the broadband photo-response. Furthermore, for longer wavelength, the charge carriers generated at lower energy distribution cannot be excited to the relative high π^* states. Instead, the excited carriers are mainly trapped in the localized states in sp^3 domains, contributing the broadband photo-response. We should point out that the performance of our FG/Gr photodetector has not been fully optimized yet. We expect that the device would also further respond to the wavelengths below 255 nm and above 4.3 μm.

Furthermore, the photocurrent and dark current can be smoothly tuned by varying the back-gate voltage V_{GS} (Figure S3 a). The transfer of photo-generated holes from FG to graphene induces p type-doping, which leads to a ~30 V up-shift of the V_{Dirac} of the FG/Gr compared to Gr/Gr. Figure S3 b

9

clearly shows a linear characteristics of I_{DS} - V_{DS} at all V_{GS} tuned from 0 to 25 V, indicating an Ohmic contact instead of a Schottky contact of the FG/Gr device. The photocurrent at different laser wavelengths, as a function of C/F ratio x, is displayed in Figure 3 j, where zero indicates the Gr/Gr device. It should be noted that we have tested tens of devices and the variance of measured data is shown in the figure. As the C/F ratio decreases, more fluorine adatoms bonded with the carbon atoms, leads to a higher degree of sp^3 re-hybridization. A larger coverage of fluorine leads to more quantum-confined sp^2 nano-domains and localized states in the system, thus leading to a higher responsivity. However, a characteristic photo-response saturation was observed at 3.75 C/F ratio, where the resulting sp^2/sp^3 nano-domains achieve their optimal size and number for the trapping of photo-excited electrons. Since the overall C/F ratio obtained from the X-ray photoelectron spectroscopy (XPS) results is 4, the density of F atoms in the FG/Gr device can be calculated to be 4.75×10^{14} cm^{-2}. In addition, a characteristic saturation of responsivity with the decrease of C/F ratio was observed. The effective absorption becomes saturated as the number of C-F bonds reaches its limit on the FG, where the absorption constant η is estimated to be 0.02 in a similar condition as reported previously.[35] Under illumination, trapped electrons in the FG forms an electric field in the direction opposite to the gate electric field, inducing the photo-gating effect.[36] Since the size/shape of sp^2 and sp^3 domains are random on FG resulting in a local non-uniformity of the electric field, we believe that the spatial non-uniformity of photo-gating effect could be further improved to obtain a higher photo-response.

It is reported that the photo-response is also attributed to other mechanisms simultaneously, including photo-thermoelectric (PTE),[37] bolometric (BOL)[38] and hot carriers effects[39]. To obtain insight into the potential contributions from thermal effects, including PTE effect from the Au/Cr

electrodes and BOL effect from FG/Gr, we calculated the responsivity (R) from these two effects by:

(1) $R_{PTE} \gg S_M(\Delta T / P_{opt})G$, where Seebeck coefficient

$$S_M = -\frac{\pi^2 k^2 T}{3q}\frac{1}{G}\frac{dG}{dV_{GS}}(\frac{dV_{GS}}{dE})_{E=E_F} \qquad (2)$$

and the temperature difference at the junction $\Delta T = P\alpha / k2\pi h$; P_{opt} is the optical power, and G is the conductance I_{DS}/V_{DS}. The R_{PTE} can be then estimated as 9.8×10^{-25} A/W; (2) $R_{BOL} = (E_a / kT^2)(\Delta T / P_{opt}) \approx 1.7 \times 10^{-4}$ A/W, where E_a is the activation energy.

Both R_{PTE} and R_{BOL} are far from the responsivity of the FG/Gr photodetector we obtained experimentally as shown in Figure 2 d. And the hot-carriers multiplications contributing to the responsivity are negligible, which will be discussed in the following section. It thus allows us to rule out the contributions from these mechanisms for generating photocurrent in our case. Moreover, it is also informative to consider a non-trap case. The density of photo-generated electrons and holes is $\Delta n = \Delta p = \varphi \tau_l$, where φ is the photon flux and τ_l is the carrier lifetime in graphene. The photocurrent can be calculated from $I_{ph} = (W / L)V_{DS}\Delta\sigma$, where W and L are the width and length of the graphene channel; the change of conductivity $\Delta\sigma = q(\mu_n + \mu_p)\Delta p$; q is the electron charge; μ_n and μ_p are the electron and hole mobility. The non-trap responsivity $R_{\text{non-trap}}$ can be then obtained as 2.46×10^{-5} A/W.

Therefore, we believe that the photo-response of the FG/Gr device is ascribed to photo-gating effects in both sp^2 and sp^3 domains. The total responsivity R consists of these two contributions R_{sp2} and R_{sp3}, with a 6.4 R_{sp3}/R_{sp2} ratio. As discussed in the previous sections, the trapping of photo-excited

11

electrons in sp^2 and sp^3 domains are due to the quantum-confinement and localized states, respectively, where the trapping time τ_{sp3} is longer than τ_{sp2} as indicated in Figure 1 b. The trapped charge density at saturation is determined by[40] $N_{sat} = \phi_{sat}\tau_S$, where the absorbed photon flux is $\phi = \eta P_{laser}\lambda / Ahc$, and τ_S is the dominant time constant from both sp^2 and sp^3 domains. η is the absorption coefficient; A is the area of illumination; h is Planck's constant; and c is the speed of light. The trapped charge density of FG at saturation N_{sat} is then calculated to be 9.8×10^{14} cm^{-2}.

Since the photocurrent is defined as the difference of I_{DS} between dark and illumination conditions, I_{ph} is equal to $I_{ph\_sp^2} + I_{ph\_sp^3}$. To differentiate these two effects, the photocurrent of FG/Gr device was measured under laser illumination with a modulated chopper frequency. It is found that a small current oscillates with chopper frequency, superimposing on a larger background current as depicted in the inset of **Figure 4** a. The black dash dot line represents the dark current. When the chopper blocks the laser, the oscillating current component (due to the trapping in sp^2 domains) disappears immediately; when the laser is totally switched off, the non-oscillating current component (due to the trapping in sp^3 domains) drifts slowly back to the dark current value. Furthermore, no modulated chopper frequency dependence of the $I_{ph\_sp^2}$ from 0 to 0.5 Hz was observed (Figure 4 a).

The transient photocurrent response to ON/OFF illumination is exhibited in Figure 4 b. The FG/Gr shows a larger photocurrent change because of the trapping of photo-excited charge carriers compared to the Gr/Gr. Across the entire tested UV to mid-IR wavelength region, the FG/Gr device consistently shows moderate switching, excellent stability and reproducibility. When the laser is turned on, the photocurrent reaches its maximum level within 80 ms and the decays in 200 ms (Figure S3 f). Despite the high photo-responsivity of our FG/Gr photodetector over a broadband range, we need to point out

that the operation speed is not very fast. The reason is the long trapped carriers lifetime in both sp^2 and sp^3 domains.[41] The improvement of operation speed to shorten the lifetime of trapped electrons while maintaining a relatively high responsivity is currently under investigation. With high responsivity and low noise current, the calculated noise equivalent power (NEP) (Figure 4 c) exhibits a promising prospect of the FG/Gr device in weak light detection. In addition, the peak specific detectivity (D*) reaches 4×10^{11} Jones (Figure 4 d), which is nearly three orders of magnitude larger than that of the Gr/Gr device.

Since the responsivity can be expressed as:

$$R = \eta \frac{\lambda q}{hc} \cdot \frac{\tau_l}{t_{tr}} \qquad (3)$$

where τ_l is the trapped carriers lifetime and t_{tr} is the carriers transit time through the device, we see that $t_{tr} = L^2 / \mu_n V_{DS}$. The responsivity against the inverse carrier transit time t_{tr} can be then obtained (Figure 4 e). The approximately linear scaling of the responsivity with μ_n and L^{-2} illustrates the performance, and the relationship between the photoconductive gain and the channel length, of the FG/Gr devices.

Although moderate impact ionization and carrier multiplication have been reported in a mono-graphene sheet with quantum dot-like arrays structure as the midgap-state-band electron trapping centers were formed and a bandgap was created.[8] We believe that there are negligible impact ionization and carrier multiplication effects in our system, which is evidenced by the gain remaining constant with the increase in incident photon energy (Figure 4 f). Figure 4 f also shows the trapped carriers lifetime as a function of incident photon energy, where the τ_l is about 0.2 s.

The performance of the FG/Gr device shows important advantages over the previous reports, as exhibited in **Figure 5**. The key metrics are also compared in Table. S1. Although the responsivity and response time of the FG/Gr photodetector are not the best, the consistent performance across the whole tested spectral range from UV to mid-IR has not been reported in the published literatures. We notice that the FG could be partially decomposed over the time despite their energetic favorability, as indicated by the statistical analysis and error bars in Figure 3. Therefore, the stability of the FG/Gr photodetector has been improved by depositing a thin high-k dielectric material, Al_2O_3 on the top of the device to passivate the FG. The Al_2O_3 protected device exhibits stable electrical characteristics. The device was evaluated by re-measuring the photo-response after exposure to the open-air environment for months.[42] The device performance was well maintained after such a long time. The responsivity was slightly improved in UV but not in VIS and IR, while the response time showed no obvious difference across the tested UV to IR wavelength range.[43] Furthermore, we believed that the patterning of FG to control the size/shape of sp^2/sp^3 nano-domains would largely influence the device performance, since the quantum-confinement in sp^2 and the localized states at sp^2/sp^3 edge can be modified. As the FG also possesses two-dimensional material's properties and can be decomposed in general ambient condition, it is an alternative candidate for next generation degradable, flexible and transparent broadband photodetectors.

In summary, we report a van der Waals heterostructure photodetector consisting of graphene and its fluorine-functionalized derivative that enhances the photo-response of graphene with broadband sensitivity. The consistent performance of the device shows broadband photo-response from UV to mid-IR with high detectivity and moderate switching speed, which can be further improved by engineering the nature of sp^3 site. The proposed scheme in this work paves the pathway towards implementing high-performance broadband graphene-based photodetectors.

Experimental Section

Graphene growth: Single crystal graphene was grown in a tube furnace (Thermo Scientific Lindberg/Blue M). Cu foil (Alfa Aesar 46365, thickness of 25 µm) was placed inside the chamber. The CVD Chamber was evacuated to lower than 0.5 Pa, and then we introduced 50 sccm H_2 to 50 Pa. The Cu foil was annealed at 1060 °C for 100 min. Next the chamber was flowed with 0.3 sccm O_2 for 10 min to reduce the nucleation density. After this step, single crystal graphene was grown in 350 sccm H_2 and 0.3 sccm CH_4 for 4 hours.[44] The multi-layer graphene was grown underneath the first layer of graphene on the Cu foil.

Graphene transfer: Before transfer, we etched the graphene grown on backside of Cu foil by O_2 plasma to avoid Cu residues between the topside and backside of graphene. After etching, graphene/Cu was spin-coated (with 500 rpm for 5s and then 4000 rpm for 60s) by polymethyl methacrylate (PMMA) (<100 µm). Then the PMMA/graphene/Cu sample was put into a Cu etching solution ($5H_2O \cdot CuSO_4$:HCl:H_2O=15.6g:50ml:50ml) for more than 12 hours to obtain the PMMA/graphene film. The film was rinsed in DI water for 1 min and followed by SC-2 etching solution (H_2O:H_2O_2:HCl=100ml:5ml:5ml) for 15 mins to remove Cu particles. Next the sample was cleaned in DI water again and placed into SC-1 etching solution (H_2O:H_2O_2:NH_4OH= 100ml:5ml:5ml) to reduce polymer residuals. PMMA/graphene was then transferred onto a SiO_2 substrate. Finally, the PMMA was washed off using dichloromethane (DCM) at 50 °C and Isopropyl Alcohol (IPA). To minimize the damage and contamination during the process, wet etching, bubble

transfer, and RCA were added to the wet etching transfer process and were compared (Figure S5). The RCA (Radio Corporation of America) added wet etching method shows the best graphene quality due to the removal of insoluble inorganic residues and heavy metal contaminants of RCA cleaning process.

Fluorographene and characterization: Single crystal graphene was fluorinated by inductively coupled plasma (ICP) system (Oxford Instrument) using SF_6 plasma. The FG/Gr heterostructure was fabricated by fluorinating multi-layer graphene with SF_6 100sccm, 5 W-50W for 1-120 min. The pressure and gas flow in the ICP reactive chamber were set to 10 mTorr and 100 sccm for the whole study. All samples were exposed to the plasma on only one side. A Renishaw® Invia system with 532 nm laser source was used for Raman characterization. The laser power was ~1mW to avoid reduction of fluorine. XPS characterization was conducted using a Thermo Scientific ESCALAB250 Xi system, with a base pressure of 7×10^{-9} mbar. An Al Kα X-ray source (1486.6 eV) was used. The pass energy was 100 eV for survey spectra and 30 eV for core level. The step size was 1 eV and 0.1 eV, respectively. However, by controling the C/F ratio *x*, we found that *x*= 3.75 results in the optimized photodetector performance over other C/F ratios. Hence, the FG with 3.75 C/F ratio is used for the FG/Gr devices. Figure S4 a illustrates the spectra from the XPS measurements of the graphene and FG, indicating that graphene has been activated by fluorine. Only the very top layer became to FG, which was verified by the Raman mapping (Figure S4 b).[45]

Device fabrication and characterization: Devices were fabricated on a commercially purchased highly *p*-doped Si wafer (Resistivity of 1~10 Ω•cm) with 100 nm SiO_2 layer on top. Gr/Gr and FG/Gr were patterned by photolithography and etched by O_2 plasma to obtain a 150 μm long and 50 μm wide ribbon. The devices were annealed for 120 min at 300 °C under H_2 before all the measurements to remove the residues and contaminants. The photocurrents were measured using an Agilent

Semiconductor Analyzer b1500. Nine lasers with the wavelength of 255 nm, 375 nm, 532 nm, 980 nm, 1319 nm, 1870 nm, 2.8 µm, 3.5 µm, 4.3 µm and irradiance from 4.83 µW/cm^2 to 11 mW/cm^2 were used to illuminate the photodetectors. The mid-infrared measurements were conducted at 77 K under 10^{-4} Torr.

Supporting Information

Supporting Information is available from the Wiley Online Library or from the author.

Acknowledgements

17

References

[1]   J. P. Clifford, G. Konstantatos, K. W. Johnston, S. Hoogland, L. Levina, E. H. Sargent, *Nat Nano* **2009**, *4*, 40.

[2]   J. Liu, D. D. Cannon, K. Wada, Y. Ishikawa, S. Jongthammanurak, D. T. Danielson, J. Michel, L. C. Kimerling, *Appl. Phys. Lett.* **2005**, *87*, 011110.

[3]   A. Poglitsch, C. Waelkens, N. Geis, H. Feuchtgruber, B. Vandenbussche, L. Rodriguez, O. Krause, E. Renotte, C. V. Hoof, P. Saraceno, *Proceedings of the Dusty & Molecular Universe A Prelude to Herschel & Alma* **2004**, *5487*, 425.

[4]   P. Peumans, A. Yakimov, S. R. Forrest, *J. Appl. Phys.* **2003**, *93*, 3693.

[5]   B. L. Carter, E. Shaw, J. T. Olesberg, W. K. Chan, T. C. Hasenberg, M. E. Flatte, *Electron. Lett.* **2000**, *36*, 1301.

[6]   J. L. Pau, J. Anduaga, C. Rivera, Á. Navarro, I. Álava, M. Redondo, E. Muñoz, *Appl. Opt.* **2006**, *45*, 7498.

[7]   C.-H. Liu, Y.-C. Chang, T. B. Norris, Z. Zhong, *Nat Nano* **2014**, *9*, 273; H. Yuan, X. Liu, F. Afshinmanesh, W. Li, G. Xu, J. Sun, B. Lian, A. G. Curto, G. Ye, Y. Hikita, Z. Shen, S.-C. Zhang, X. Chen, M. Brongersma, H. Y. Hwang, Y. Cui, *Nat Nano* **2015**, *10*, 707.

[8]   B. Y. Zhang, T. Liu, B. Meng, X. Li, G. Liang, X. Hu, Q. J. Wang, *Nat Commun* **2013**, *4*, 1811.

18

[9]   J. M. Bioucas-Dias, A. Plaza, "An overview on hyperspectral unmixing: Geometrical, statistical, and sparse regression based approaches", presented at *Geoscience and Remote Sensing Symposium (IGARSS), 2011 IEEE International*, 24-29 July 2011, 2011.

[10]   J. C. Harsanyi, C. Chang, *IEEE Transactions on Geoscience & Remote Sensing* **1994**, *32*, 779.

[11]   S. N. Chesnokov, D. E. Dolzhenko, I. I. Ivanchik, D. R. Khokhlov, *Infrared Physics & Technology* **1994**, *35*, 23.

[12]   H. Kind, H. Yan, B. Messer, M. Law, P. Yang, *Adv. Mater.* **2002**, *14*, 158.

[13]   M. E. Schaffer, P. A. Mitkas, *IEEE J. Sel. Top. Quantum Electron.* **1998**, *4*, 856.

[14]   G. Konstantatos, J. Clifford, L. Levina, E. H. Sargent, *Nat Photon* **2007**, *1*, 531.

[15]   R. Koeppe, A. Neulinger, P. Bartu, S. Bauer, *Opt. Express* **2010**, *18*, 2209.

[16]   C. J. Chen, K. K. Choi, W. H. Chang, D. C. Tsui, *Appl. Phys. Lett.* **1998**, *72*, 7.

[17]   V. I. Sankin, V. P. Chelibanov, *physica status solidi (a)* **2001**, *185*, 153.

[18]   D. L. Freese, A. Vandenbroucke, D. Innes, F. W. Y. Lau, D. F. C. Hsu, P. D. Reynolds, C. S. Levin, *Med. Phys.* **2015**, *42*, 305.

[19]   A. Mäkynen, T. Rahkonen, J. Kostamovaara, *Sensors and Actuators A: Physical* **1998**, *65*, 45.

[20]   M. B. Gray, D. A. Shaddock, C. C. Harb, H.-A. Bachor, *Rev. Sci. Instrum.* **1998**, *69*, 3755.

[21]   L. Vicarelli, M. S. Vitiello, D. Coquillat, A. Lombardo, A. C. Ferrari, W. Knap, M. Polini, V. Pellegrini, A. Tredicucci, *Nat Mater* **2012**, *11*, 865.

[22]   A. K. Geim, K. S. Novoselov, *Nat Mater* **2007**, *6*, 183; K. S. Kim, Y. Zhao, H. Jang, S. Y. Lee, J. M. Kim, K. S. Kim, J.-H. Ahn, P. Kim, J.-Y. Choi, B. H. Hong, *Nature* **2009**, *457*, 706.

[23]   K. S. Novoselov, A. K. Geim, S. V. Morozov, D. Jiang, M. I. Katsnelson, I. V. Grigorieva, S. V. Dubonos, A. A. Firsov, *Nature* **2005**, *438*, 197; A. H. Castro Neto, F. Guinea, N. M. R. Peres, K. S. Novoselov, A. K. Geim, *Rev. Mod. Phys.* **2009**, *81*, 109.

[24]   L. Ju, B. Geng, J. Horng, C. Girit, M. Martin, Z. Hao, H. A. Bechtel, X. Liang, A. Zettl, Y. R. Shen, F. Wang, *Nat Nano* **2011**, *6*, 630.

[25]   M. Furchi, A. Urich, A. Pospischil, G. Lilley, K. Unterrainer, H. Detz, P. Klang, A. M. Andrews, W. Schrenk, G. Strasser, T. Mueller, *Nano Lett.* **2012**, *12*, 2773.

[26]   X. Gan, R.-J. Shiue, Y. Gao, I. Meric, T. F. Heinz, K. Shepard, J. Hone, S. Assefa, D. Englund, *Nat Photon* **2013**, *7*, 883.

[27]   W. Zhang, C.-P. Chuu, J.-K. Huang, C.-H. Chen, M.-L. Tsai, Y.-H. Chang, C.-T. Liang, Y.-Z. Chen, Y.-L. Chueh, J.-H. He, M.-Y. Chou, L.-J. Li, *Sci. Rep.* **2014**, *4*, 3826.

[28]   G. Konstantatos, M. Badioli, L. Gaudreau, J. Osmond, M. Bernechea, F. P. G. de Arquer, F. Gatti, F. H. L. Koppens, *Nat Nano* **2012**, *7*, 363.

[29]   O. Leenaerts, H. Peelaers, A. D. Hernández-Nieves, B. Partoens, F. M. Peeters, *Phys. Rev. B* **2010**, *82*, 195436; H. Şahin, M. Topsakal, S. Ciraci, *Phys. Rev. B* **2011**, *83*, 115432.

[30]   J. O. Sofo, A. M. Suarez, G. Usaj, P. S. Cornaglia, A. D. Hernández-Nieves, C. A. Balseiro, *Phys. Rev. B* **2011**, *83*, 081411.

[31]   Z. H. Ni, L. A. Ponomarenko, R. R. Nair, R. Yang, S. Anissimova, I. V. Grigorieva, F. Schedin, P. Blake, Z. X. Shen, E. H. Hill, K. S. Novoselov, A. K. Geim, *Nano Lett.* **2010**, *10*, 3868.

[32]   J.-A. Yan, L. Xian, M. Y. Chou, *Phys. Rev. Lett.* **2009**, *103*, 086802.

[33]   C.-T. Chien, S.-S. Li, W.-J. Lai, Y.-C. Yeh, H.-A. Chen, I. S. Chen, L.-C. Chen, K.-H. Chen, T. Nemoto, S. Isoda, M. Chen, T. Fujita, G. Eda, H. Yamaguchi, M. Chhowalla, C.-W. Chen, *Angew. Chem.* **2012**, *124*, 6766.

[34]   K. Thiyagarajan, A. Ananth, B. Saravanakumar, Y. S. Mok, S.-J. Kim, *Carbon* **2014**, *73*, 25; K. Thiyagarajan, B. Saravanakumar, S.-J. Kim, *ACS Appl. Mater. Interfaces* **2015**, *7*, 2171.

[35]   R. R. Nair, W. Ren, R. Jalil, I. Riaz, V. G. Kravets, L. Britnell, P. Blake, F. Schedin, A. S. Mayorov, S. Yuan, M. I. Katsnelson, H.-M. Cheng, W. Strupinski, L. G. Bulusheva, A. V. Okotrub, I. V. Grigorieva, A. N. Grigorenko, K. S. Novoselov, A. K. Geim, *Small* **2010**, *6*, 2877.

[36]   L. Britnell, R. M. Ribeiro, A. Eckmann, R. Jalil, B. D. Belle, A. Mishchenko, Y.-J. Kim, R. V. Gorbachev, T. Georgiou, S. V. Morozov, A. N. Grigorenko, A. K. Geim, C. Casiraghi, A. H. C. Neto, K. S. Novoselov, *Science* **2013**, *340*, 1311.

[37]   X. Cai, A. B. Sushkov, R. J. Suess, M. M. Jadidi, G. S. Jenkins, L. O. Nyakiti, R. L. Myers-Ward, S. Li, J. Yan, D. K. Gaskill, T. E. Murphy, H. D. Drew, M. S. Fuhrer, *Nat Nano* **2014**, *9*, 814.

[38]   N. Kurra, V. S. Bhadram, C. Narayana, G. U. Kulkarni, *Nanoscale* **2013**, *5*, 381.

[39]   N. M. Gabor, J. C. W. Song, Q. Ma, N. L. Nair, T. Taychatanapat, K. Watanabe, T. Taniguchi, L. S. Levitov, P. Jarillo-Herrero, *Science* **2011**, *334*, 648.

[40]   M. M. Furchi, D. K. Polyushkin, A. Pospischil, T. Mueller, *Nano Lett.* **2014**, *14*, 6165.

[41]   A. Cortijo, M. A. H. Vozmediano, *Nucl. Phys. B* **2007**, *763*, 293; Y. A. Sitenko, N. D. Vlasii, *Nucl. Phys. B* **2007**, *787*, 241.

[42]   Y. Xu, A. Ali, K. Shehzad, N. Meng, M. Xu, Y. Zhang, X. Wang, C. Jin, H. Wang, Y. Guo, Z. Yang, B. Yu, Y. Liu, Q. He, X. Duan, X. Wang, P.-H. Tan, W. Hu, H. Lu, T. Hasan, *Advanced Materials Technologies* **2016**, 1600241.

[43]   X. Wan, Y. Xu, H. Guo, K. Shehzad, A. Ali, Y. Liu, J. Yang, D. Dai, C.-T. Lin, L. Liu, H.-C. Cheng, F. Wang, X. Wang, H. Lu, W. Hu, X. Pi, Y. Dan, J. Luo, T. Hasan, X. Duan, X. Li, J. Xu, D. Yang, T. Ren, B. Yu, *npj 2D Materials and Applications* **2017**, *in press*.

[44]   P. Zhao, Y. Cheng, D. Zhao, K. Yin, X. Zhang, M. Song, S. Yin, Y. Song, P. Wang, M. Wang, Y. Xia, H. Wang, *Nanoscale* **2016**, *8*, 7646.

[45]   Q. Li, H. Chou, J.-H. Zhong, J.-Y. Liu, A. Dolocan, J. Zhang, Y. Zhou, R. S. Ruoff, S. Chen, W. Cai, *Nano Lett.* **2013**, *13*, 486.
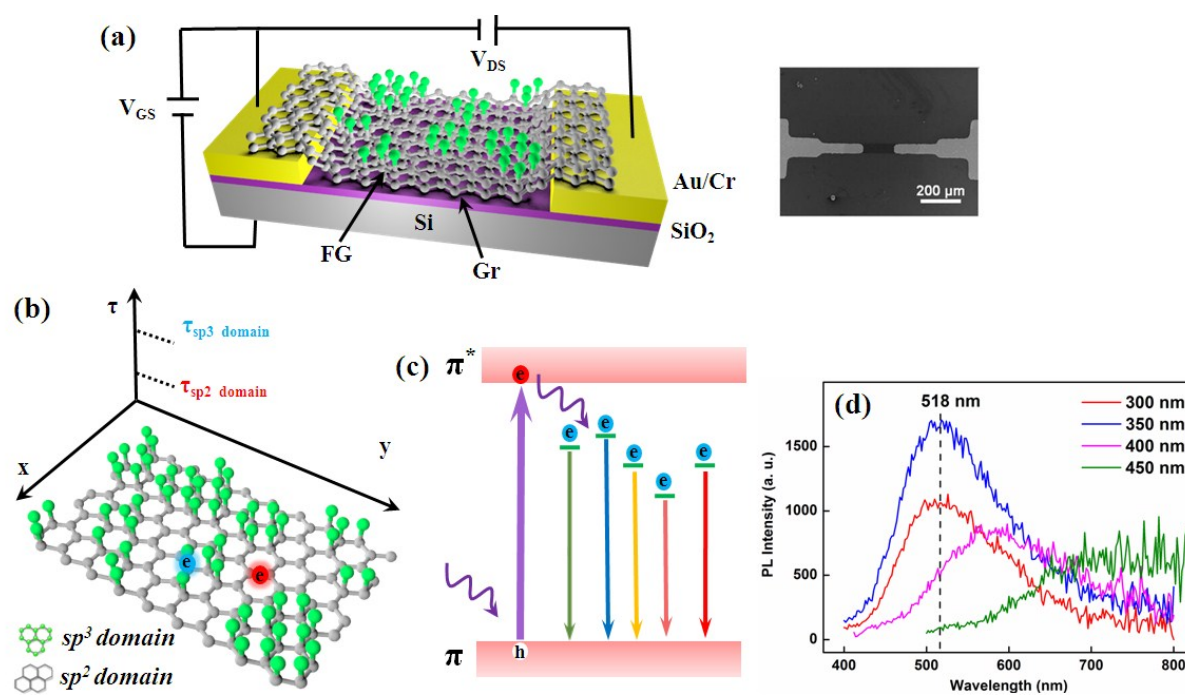
Figure 1. Device structure and PL characterization. a) Schematic FG/Gr photodetector structure and the top-view SEM image. b) Schematic sp^3 and sp^2 domains on FG with indicated trapped carriers lifetime, and (d) corresponding optical transitions. e) PL spectra of the FG at different excitation wavelengths.
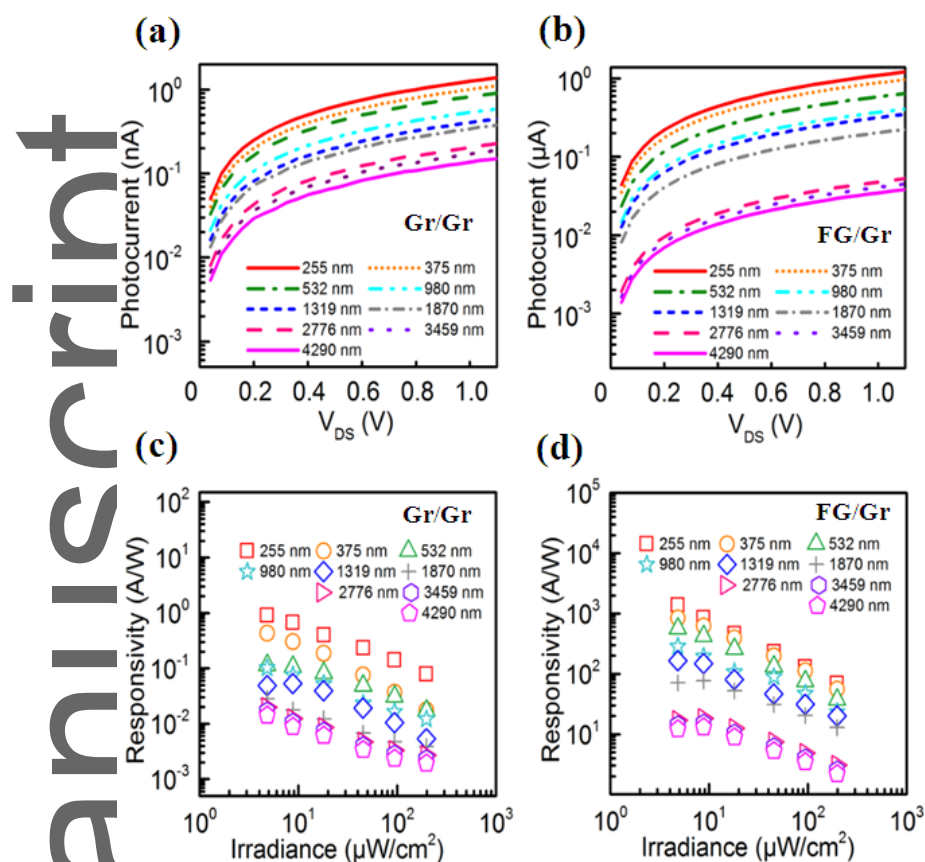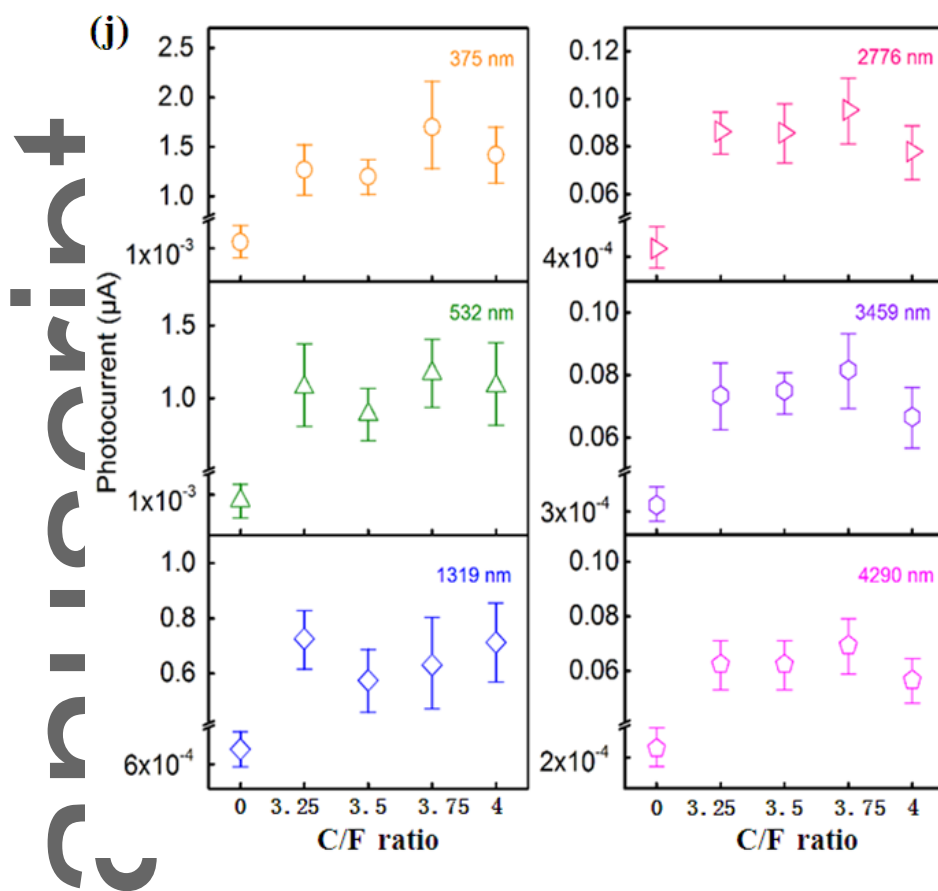
Figure 2. Photo-response results. The photocurrent *ΔI* as a function of V_{DS} of Gr/Gr (a) and FG/Gr (b) devices at different laser wavelengths with a fixed irradiance of 198 µW/cm^2. Responsivity as a function of the laser irradiance of Gr/Gr (c) and FG/Gr (d) devices at different laser wavelengths with V_{DS} =1V and V_{GS} = 28V.
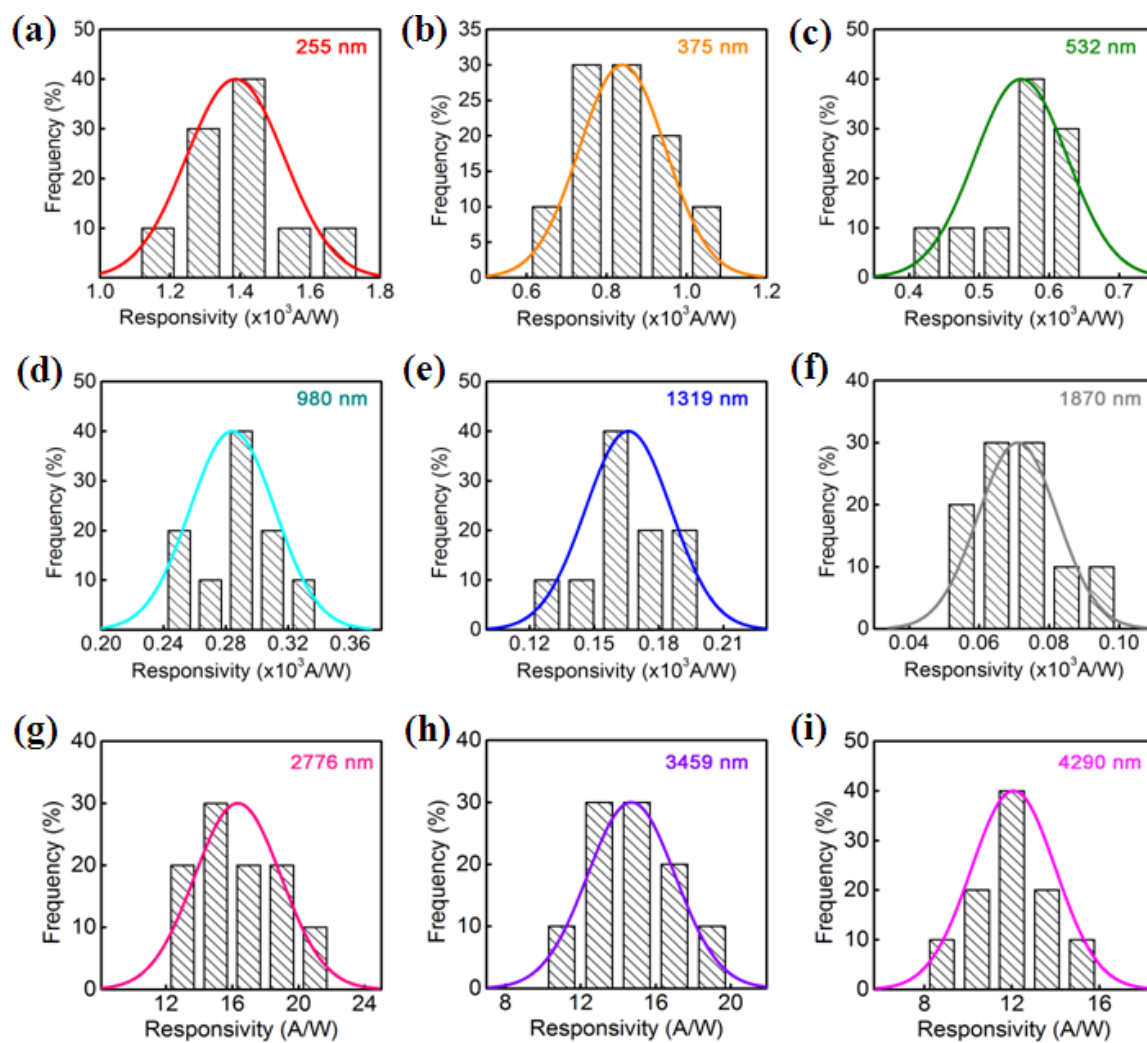
**Figure 3.** Statistical responsivities. Frequency of responsivity at 255 nm (a), 375 nm (b), 532 nm (c), 980 nm (d), 1319 nm (e), 1870 nm (f), 2776 nm (g), 3459 nm (h) and 4290 nm (i) laser wavelength of FG/Gr devices with 3.75 C/F ratio; the laser irradiance was 4.83 μW/cm² (11 mW/cm² for mid-IR lasers), V_{DS} = 1V, V_{GS} = 28V. j) Photocurrent as a function of the C/F ratio at these laser wavelengths with a irradiance of 198 μW/cm² (11 mW/cm² for mid-IR lasers), where the zero represents Gr/Gr device and the error bar indicates the variance of multiple devices of the same type.
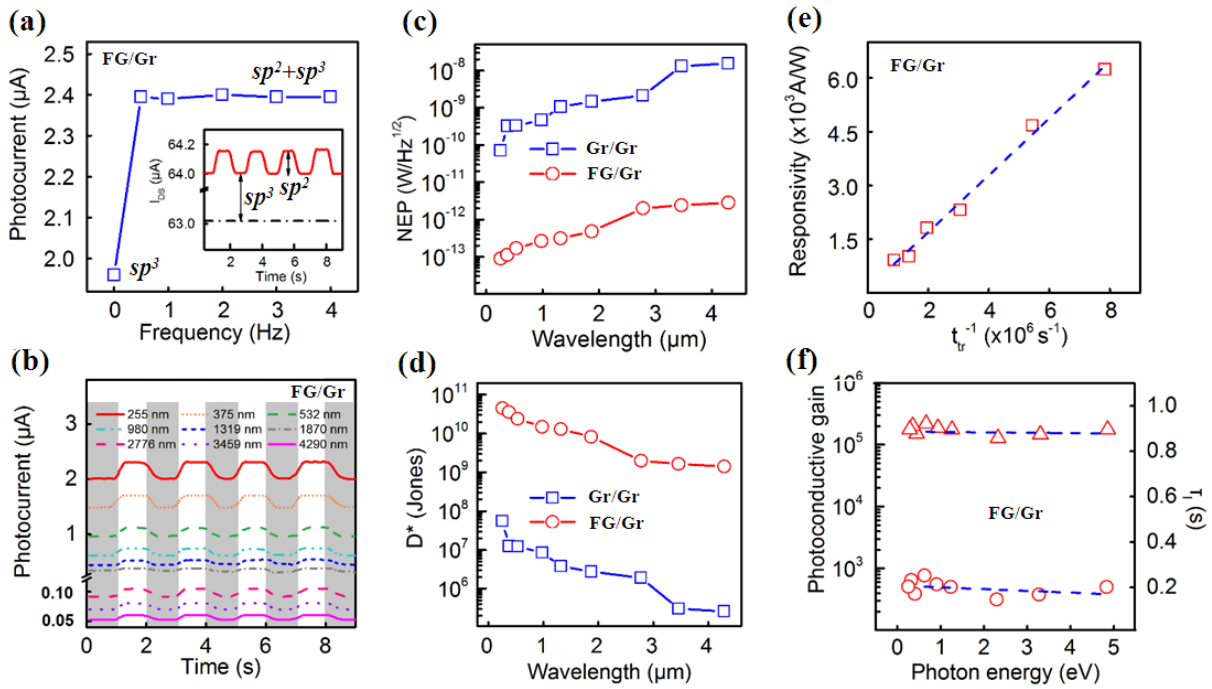
Figure 4. Key metrics of the devices. a) Photocurrent as a function of the chopper frequency. The data point at zero frequency indicates the sp^3 domain photo-gating. Inset shows that I_{DS} time response in the dark condition (dash dot black line) and under illumination (solid red line), where λ = 532 nm, P_{laser} = 198 μWcm^{-2}, and chopper frequency f = 0.5 Hz. b) The time response of FG/Gr photodetector at different laser wavelengths, where V_{DS} = 1 V and V_{GS} = 28 V; lasers were OFF at gray area and ON at white area. The calculated NEP (c) and D* (d) of Gr/Gr and FG/Gr photodetector. e) Responsivity as a function of inverse carrier transit time t_{tr}^{-1}. f) The photoconductive gain and carrier lifetime as a function of photon excitation energies. The triangular and circular symbols represent the photoconductive gain and carrier lifetime, respectively. The blue dash lines in (e) and (f) represent a linear fitting.
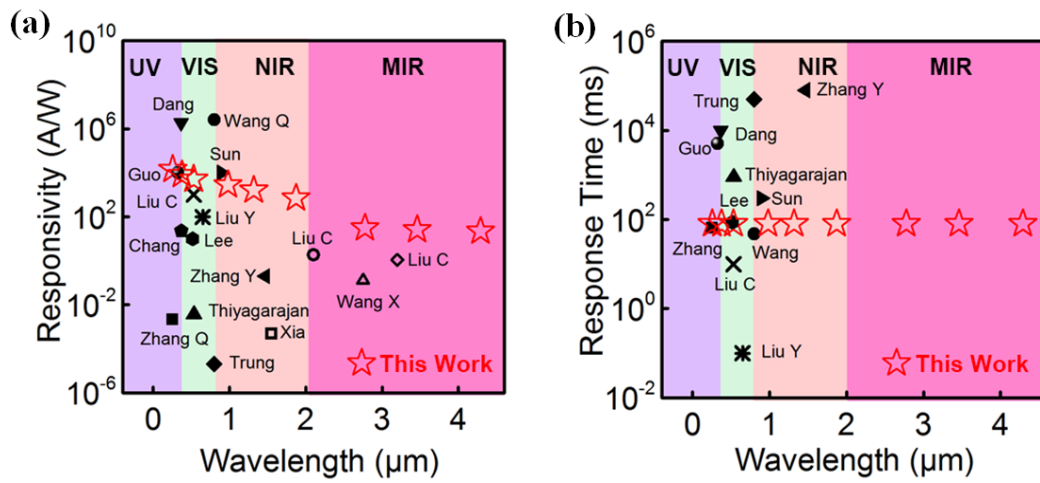
Figure 5. Responsivity (a) and response time (b) of the FG/Gr photodetector compared to those of related photodetectors reported in the literature.

The table of contents entry

A photodetector based on van der Waals heterostructures of graphene and its fluorine-functionalized derivative is presented. It consistently shows broadband photo-response from 255 nm to 4.3 μm wavelength range. The broadband photodetection is attributed to the synergistic effects of the spatial non-uniform collective quantum confinement of sp^2 domains, and the trapping of photo-excited charge carriers in the localized states in sp^3 domains.
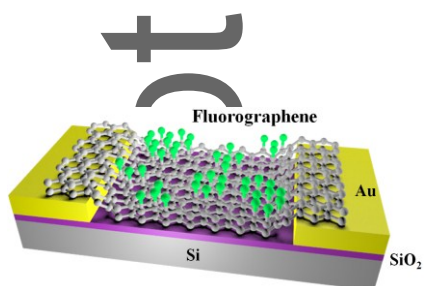
Keyword: fluorographene, broadband, photodetector, ultraviolet, mid-infrared

Yang Xu*, Weida Hu*

Title: Broadband Fluorographene Photodetector

ToC figure

Author Manuscript